ELSEVIER

Clinical Neurophysiology 113 (2002) 1209–1226

www.elsevier.com/locate/clinph

Semantic geodesic maps: a unifying geometrical approach for studying the structure and dynamics of single trial evoked responses

N.A. Laskaris, A.A. Ioannides*

Laboratory for Human Brain Dynamics, Brain Science Institute, Riken, Wako-shi 351-0198, Japan

Accepted 16 April 2002

Abstract

Objectives: A general framework for identifying and describing structure in a given sample of evoked response single-trial signals (STs) is introduced. The approach is based on conceptually simple geometrical ideas and enables the convergence of *pattern analysis and non-linear time series* analysis.

Methods: Classical steps for analyzing the STs by waveform are first employed and the ST-analysis is transferred to a multidimensional space, the feature space, the geometry of which is systematically studied via multidimensional scaling (MDS) techniques giving rise to *semantic maps*. The structure in the feature space characterizes the *trial-to-trial variability* and this is utilized to probe functional connectivity between two brain areas. The underlying dynamic process responsible for the emerged structure can be described by a multidimensional trajectory in the feature space. This in turn enables the detection of dynamical interareal coupling as similarity between the corresponding trajectories.

Results and conclusions: The utility of semantic maps was demonstrated using magnetoencephalographic data from a simple auditory paradigm. The coupling of ongoing activity and evoked response is vividly demonstrated and contrasted with the apparent deflection from zero baseline that survives averaging. Prototypes are easily identified as the end points of distinct paths in the semantic map representation, and their neighborhood is populated by STs with distinct properties not only in the latencies where the evoked response is expected to be strong, but also and very significantly in the prestimulus period. Finally our results provide evidence for interhemispheric binding in the (4–8 Hz) range and dynamical coupling at faster time scales.

Keywords: Single trial analysis; Visualization; Non-linear dynamics; Functional connectivity; Magnetoencephalography; Auditory evoked responses

1. Introduction

The traditional approach to characterize the evoked response is to perform ensemble averaging and record for each site, the polarity, latency and amplitude of the major deflections of the average waveform. The ensemble average usually includes a complex of partially overlapping components reflecting different processing stages along the neural pathways. However, due to the non-stationary character of the response generation mechanism, these components are usually smeared after averaging, and the final estimation will be only a coarse summary, or worse distortion, of the events that took place during the recording session (Liu and Ioannides, 1996).

To advance beyond ensemble averaging it is necessary to deal with the low signal-to-noise ratio (SNR) of the evoked responses which are always embedded within (and quite often coupled with) the ongoing brain activity. An evoked response does not depend solely on the stimulus physical characteristics, but also on many other factors like subject's performance and psychophysiological state. Improvement in the analysis of single-trial signals (STs) is also required for the study of interactions between brain areas (Gray, 1999; Ioannides et al., 2000; Leocani et al., 2001).

The analysis of evoked responses has been traditionally supported by *pattern analysis* methodologies (Donchin and Heffley, 1978; Gath et al., 1985). The main objective is the identification of structure in the data (Geva and Pratt, 1994; Zouridakis et al., 1997a,b; Lange et al., 2000; Hoppe et al., 2000). To this end, features are extracted from the individual ST-patterns (i.e. ST-waveforms) and *classification/clustering* techniques are employed to split the record of evoked responses to homogeneous groups of ST patterns sharing similar morphological characteristics (Geva, 1998). However, the low SNR makes the feature-selection and feature-extraction tasks non-trivial. The feature-extraction

* Corresponding author. Tel.: +81-48-467-9730; fax: +81-48-467-9731.
E-mail address: ioannides@postman.riken.go.jp (A.A. Ioannides).

1388-2457/02/$ - see front matter
PII: S1388-2457(02)00124-4

CLINPH 2001131

step can be guided by the pattern of the averaged response (Lange et al., 1997) or performed, in a fully unsupervised manner, via principal component analysis (PCA) (Geva and Pratt, 1994).

Techniques for analyzing ST-responses have been biased by the transient waveshape seen in the averaged response. Possible interdependence between successive ST-responses, non-linear interaction of the response and the ongoing brain waves and any causal relationship between prestimulus activity and the response are often overlooked (Arieli et al., 1996; Ioannides et al., 1998; Karakas et al., 2000). Powerful techniques to characterize the evolution of brain activity from a continuous-mode time series recorded at a single site have been developed in *non-linear dynamics* (Pritchard and Duke, 1995; Burioka et al., 2001; Kowalik et al., 2001; Lee et al., 2001), where also efficient numerical methods, well suited to the oscillatory nature of the measured signals, have been introduced to study the *dynamical interdependence* between brain areas (Arnhold et al., 1999). Our work brings together ideas from pattern analysis and non-linear dynamics in a unified geometrical approach for ST-analysis, which is both model-free and general.

The STs are analyzed based on their waveforms and this endows the approach with a great generality since, by modifying the feature extraction step, a rich exploration can be achieved. The approach is multivariate in nature and therefore can cope with the realistic case of interrelate features (Mardia et al., 1979). With the feature-extraction step the ST-patterns, from one recording site, can be represented by points in a (possibly) high dimensional vector space, the *feature-space*. The identification of structure in the data is then formulated as detection of the deterministic-skeleton of the point sample or as delineation of the signal related *manifold* (i.e. constrained-surface) of the point distribution in the feature-space. *The first objective* of this work is to introduce efficient ways to represent the structure of the point sample in a parsimonious, but yet meaningful way. Dimensionality reduction techniques, with a structure-preserving character, are suggested for producing an accessible image of the point-sample. *The second objective* is to suggest a general statistical scheme that quantifies the coherence in structure between two feature-spaces and can be used to detect (upon proper feature-selection) functional connectivity between brain areas. *The final objective* is to highlight the common geometrical ground shared by both *pattern analysis* and *non-linear time series analysis*: the multidimensional trajectories describing the brain's activity evolution trace paths through the *feature space*. This observation suggests a straightforward way to trace back the history of the observed structure in feature space, in order to understand better the dynamics of the response generation.

The paper has been divided into two parts. Section 2 introduces the different aspects of the unifying geometrical approach. Section 3 presents the results from analysing M100 evoked responses. The Appendices include all the necessary algorithmic steps for understanding the technical details of the approach and facilitating a direct implementation.

2. The geometric approach

2.1. Feature-space construction and multidimensional scaling

Let $x_i(t)$, $i = 1, \ldots, N$; $t = 1 \times T_s, 2 \times T_s, \ldots$, the ith scalar ST-signal collected at a single recording site with sampling frequency f_s ($T_s = 1/f_s$). The ensemble average is first computed and based on its pattern a set of latencies is selected. In the simplest case this set is a sequence of p time points around the latency of the most prominent deflection. The chain of signal-values at these latencies, called hereafter segment, will constitute the set of features extracted from each ST-waveform. In this way the feature vector (FV) extracted from the ith ST pattern takes the form of a p-dimensional vector

$$X_i = [x_i[t_1],\ x_i[t_1 + T_s],\ x_i[t_1 + 2 \times T_s],\ \ldots,\ x_i[t_1 + (p-1) \times T_s]],$$

and the given record of ST-signals can be treated as a collection of points $\{P_i\}_{i=1:N}$ populating the so-called feature space and represented by the data-matrix $\mathbf{X}_{[N \times p]} = [X_1 \vdots X_2 \vdots \ldots \vdots X_N]$. The previous scheme can easily be extended to incorporate advanced feature-extraction steps (e.g. via multirate filtering) and to combine distinct or overlapping components of the evoked response.

The geometrical relationships between the points are implicitly contained in the inter-point *distance matrix* $\mathbf{D}_{[N \times N]}$

$$D(i, j) = \|X_i - X_j\|_{L_2}, \qquad \|X_j\|_{L_2} = \sqrt{X_i \cdot X_i^T} = \sqrt{\sum_{k=0}^{p-1} (x_i(t_1 + kT_s))^2}. \quad (1)$$

A condensed representation can be achieved in simple matrix operations applied to $\mathbf{D}$ (see Appendix A) using classical (*metric*) multidimensional scaling (MDS). This distance preserving projection technique produces the image of the point cloud $\{P_i\}_{i=1:N}$ in a r-dimensional space ($r < p$) (Mardia et al., 1979; Wackermann and Matousek, 1998). The resulting low dimensional space is denoted hereafter as the *reduced feature-space*, and the point images in that space by $\mathbf{Y}_{[N \times r]} = \mathrm{MDS}_r(\mathbf{D})$.

MDS plays for *proximity data* (i.e. data in the format of $\mathbf{D}$) a role analogous to the role of PCA for *vectorial data* (i.e. data in the format of $\mathbf{X}$). The same line of reasoning that supports the use of PCA and singular value decomposition (SVD) for noise elimination over repeated ST-patterns (Donchin and Heffley, 1978; Geva and Pratt, 1994) can therefore support the idea that this low-dimensional projection constitutes enhanced, in terms of SNR, representation of the point structure. In this sense, the reduced feature-space is the subspace that portrays the trial-to-trial variability of a specific segment in a parsimonious and robust way. The concepts of feature-space and reduced feature-space are

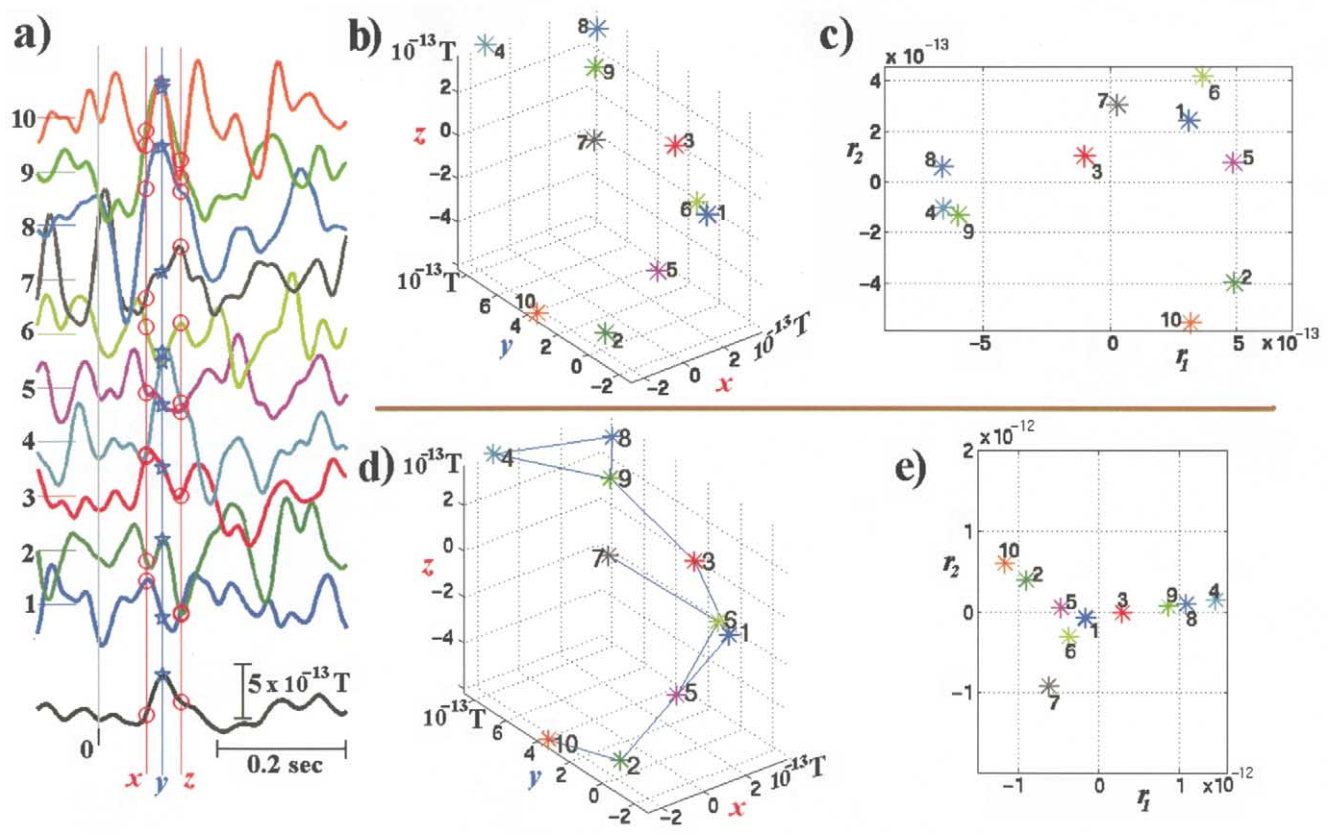

Fig. 1. (a) Feature extraction step for a ST-sample of 10 M100 auditory responses recorded from right hemisphere: the ensemble average waveform has been computed (black curve at the bottom) and a triplet of latencies around its peak has been selected; the signal-values at these latencies denoted by the vertical lines constitute the FV for each ST. (b) Feature space construction: the ST-sample is represented as a point sample in a 3-dimensional space. (c) Reduced feature space computation: an image of the point sample in a space of two dimensions is derived via classical MDS. (d) Nearest neighbor graph formation: by connecting with straight-line segments these points which are closer than ϵ (selected as the average interpoint distance). (e) Unfolding the graph on a plane.

demonstrated, via Figs. 1a–c, in the case of a ST-sample consisting of ten STs.

2.2. Application of graph theory in the feature space and isomap

The intrinsic geometry that governs the *geodesic manifold* of the point distribution can be emphasized by the incorporation of *graph-theoretic* steps prior to the application of MDS (Tenenbaum et al., 2000). The emerged dimensionality reduction technique, named *isomap*, comprises simple algorithmic steps (Appendix B), that transform the original matrix **D** to **GD** which contains the geodesic interpoint distances. In brief, *graph theory* is engaged directly in the feature space by building the *nearest-neighbor graph* over the given point sample. Each point is treated as a node of this graph, while each straight-line segment connecting two of these points being closer than ϵ is treated as an edge of it (Fig. 1d). Using this graph the *geodesic* interpoint distances are computed as the shortest paths between each pair of points. The MDS is then applied, $\mathbf{Y} = \mathrm{MDS}_r(\mathbf{GD}^{\epsilon})$, to produce the image of the original point-cloud in a reduced feature space (Fig. 1e). Isomap can be thought of as a computationally efficient graph-flattening technique that can learn a broad class of non-linear manifolds.

2.3. The appending technique: understanding the ST-sample structure through its MDS-based image

The point configuration computed in a low dimensional reduced feature space, e.g. with $r = 2$, can be used for understanding the structure of the ST-sample since it enables the visualization of the original space structure. Since MDS is a distance-preserving projection mechanism, the basic notions regarding the context of distance between a pair of FVs still hold in the reduced feature space. More specifically, *in the case of classical MDS* the interpretation of the obtained map can be based on the following rules of thumb. The length of Y_i, that is its distance from the coordinate-system origin, portrays the distance between the corresponding FV X_i and the average of the FVs (i.e. the FV of the averaged ST-segment). The angular distance between Y_i and Y_j, reflects mainly the phase-differences between the corresponding ST-segments. Finally, the distance between two points lying on the same line extended from the origin

reflects the difference in root mean-square (RMS) value between the corresponding ST-segments. *In the case of isomap* the point-diagram is not so easily interpreted, due to the graph-flattening step. Both classic MDS and isomap techniques produce maps reflecting only the relative relationships between the FVs, because information is lost about absolute measures in each neighborhood in the (reduced) feature space. In order to enhance the interpretability of these point-diagrams the *appending technique* is introduced. It acts like a pathfinder and transforms the computed maps to *semantic maps*.

The basic idea is to trace on the given map the images from a sequence of known patterns (and hence known FVs) that can serve as tags on the different map regions. This is accomplished using a standard procedure (Gower, 1968) that inserts in the reduced feature space the image of a further FV X^{app} in such a way that the geometrical relationships between it and $\{X_i\}_{i=1:N}$ will be reflected in the relationships between the appended image Y^{app} and the images $\{Y_i\}_{i=1:N}$. This procedure defines a mapping from feature space to reduced feature space that in the sequel is denoted by $Y^{app} = F_{appending}(X^{app}, \{X_i\}_{i=1:N})$ and can be executed efficiently in a batch-mode for a collection of FVs to be appended (see Appendix C).

2.4. Extracting qualitative dynamics via the appending technique

The state of a dynamical system at any time t can be specified by a vector $X(t)$ in the *state-space*, which is the space spanned by all the dynamic variables of the system. The successive vectors follow a trajectory in this space forming a geometric object that completely represents the dynamics of the system. When only a single scalar time series corresponding to a measured variable of the system is available, numerical procedures under the term *state-space reconstruction* can be employed to transform the signal, $x(t)$, to the trajectory characterizing the source of the signal (Abarbanel, 1996). The most popular procedure, *time-delay embedding*, is based on the formation of *delay-vectors*

$${}_eX(t) = [x[t - (d_e - 1) \times T_e],\ \ldots,\ x[t - 2 \times T_e],\ x[t - T_e],\ x[t]],$$

as approximations of the non-accessible state vectors $X(t)$, where the *delay-time* T_e is an integer multiple of the sampling time T_s and d_e is the *embedding dimension*. It is easy to see that if the times series corresponds to the ith ST scalar signal and $T_e = T_s$ & $d_e = p$, the delay vector runs through the feature-space and specifically ${}_eX_i(t_1 + p - 1) = X_i$, i.e. with T_e & d_e selected in this way, the feature space is the reconstructed state-space populated only by the points which correspond to stroboscopic snapshots of the dynamic process.

SVD has been used to project high dimensional trajectories reconstructed from electroencephalogram (EEG) signal onto an easier to visualize 2–3 dimensional space (Pritchard and Duke, 1995; Meng et al., 2001). The appending technique provides a robust and computationally efficient extension of this idea by projecting the high dimensional trajectories onto a low-dimensional and *meaningful* terrain. Using the ensemble of FVs $\{X_j\}_{j=1:N}$ as a meaningful reference-grid (semantic grid), the trajectory reconstructed from the ith ST scalar $x_i(t)$ and tabulated in

$$T_{i_{[(k_1+k_2+1)\times p]}} = [{}_eX_i(t_1 - k_1)\vdots \ldots \vdots {}_eX_i(t_1)\vdots \ldots \vdots {}_eX_i(t_1 + k_2)],\ k_1,\ k_2 \in N$$

can be traced on the corresponding low-dimensional semantic map (i.e. in the reduced feature space) as the sequence of vectors $\mathbf{Y_i^{app}} = F_{appending}(\mathbf{T_i},\ \{X_j\}_{j=1:N})$The left top corner of Fig. 2 shows such a trajectory reconstructed from a ST and 'appended' onto the map of Fig. 1c. The suggested visualization scheme provides a directly interpretable image of the evoked response generation dynamics and as we will show later allows us to contrast distinct dynamic modes within a set of ST-signals or to contrast each of them with the averaged response.

2.5. Structural association of two feature-spaces via Hubert's Γ statistic

Hubert's Γ statistic was originally devised to compare two different clustering structures (in time and space), to contrast the outputs from two different cluster analysis algorithms applied to the same data or to assess the fit between proximity data and a priori structures (Jain and Dubes, 1988). This statistic was introduced for handling *proximity matrices*. The notion of *proximity* is very broad. It is defined as every positive symmetric measure for which the larger numerical values are assigned to the more dissimilar object pairs and therefore includes the Euclidean distance as a special case.

Given two proximity matrices ${}^{A}\mathbf{\Delta}_{[N\times N]}$ and ${}^{B}\mathbf{\Delta}_{[N\times N]}$ on the same *objects*, the Hubert's Γ statistic is defined by the *point serial correlation* of them:

$$\Gamma = \sum_{i=1}^{N-1} \sum_{j=i+1}^{N} {}^{A}\Delta^{B}_{(i,j)}\Delta_{(i,j)} \tag{2}$$

and in the normalized form Γ_n (see Appendix D) is the sample correlation coefficient between the entries of the two matrices. The range of Γ depends on the ranges of values in the proximity matrices and on the number of entries, while Γ_n ranges always between −1 and 1. Unusually large absolute values of this statistic suggest that the two matrices agree with each other.

In the present framework the features extracted from each ST evoked response are considered as images of attributes of an abstract object. In this way the distance matrices computed in two feature-spaces, which might have been constructed via an entirely different feature-extraction step from distinct time-series, correspond to proximity matrices of the different representations of the abstract objects. Adopting this point of view, Hubert's methodology can be used to reveal stimulus induced coherence in different ST data structures. It appears as a unifying test for functional

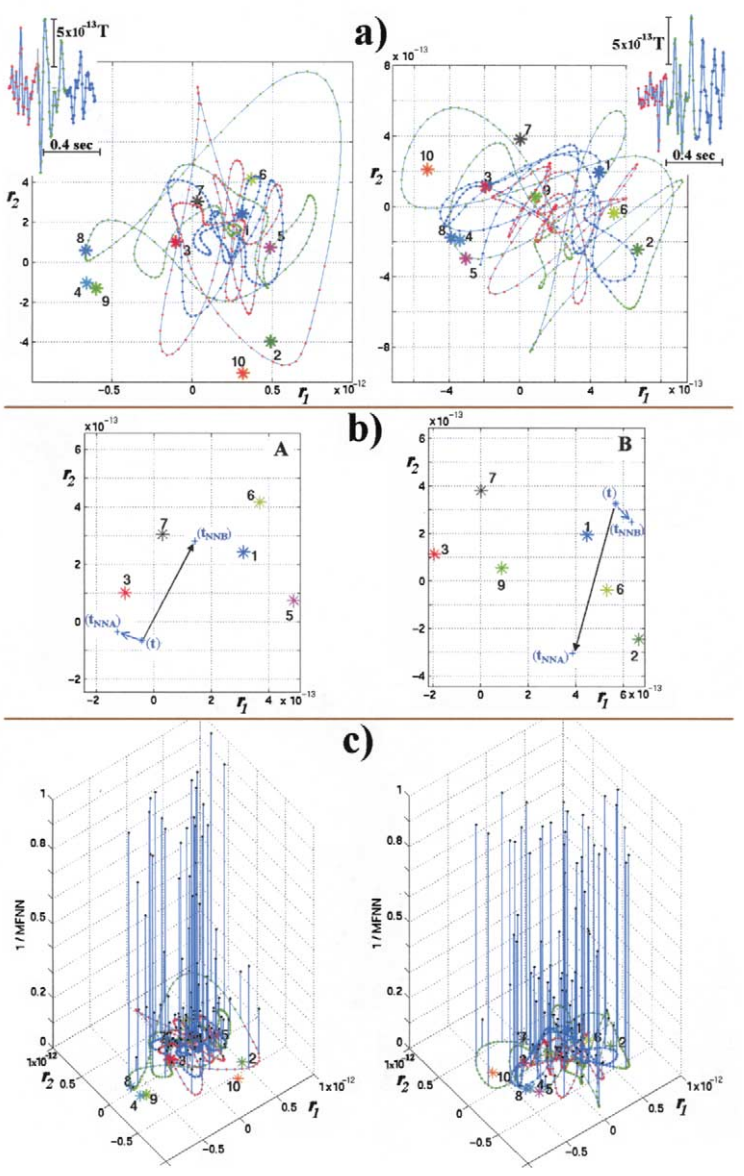

Fig. 2. Computation of the MFFN parameter in the reduced feature space; left (right) column corresponds to a signal recorded from left (right) hemisphere. (a) The trajectory reconstructed from each of the two simultaneously recorded signals during the 8th ST response has been drawn in the corresponding reduced feature space using the appending technique. (b) The MFNN parameter, associated with each time instant t, is computed using the depicted vector lengths. (c) The MFNN parameter can be plotted as a function of the position in the reduced feature space, providing information about the evolution of the dynamical coupling as the system runs along the different segments of its trajectory.

covariation (with respect to some stimulus presentation) in two ST-samples recorded simultaneously from different brain areas. This can be justified by the following facts. First, Hubert's test has proven to be the generalization/extension to multivariate data of well known statistical tests for *Bivariate association* (Hubert and Schultz, 1976), like the *Spearman's correlation,* which have previously been employed for assessing functional connectivity between brain areas (e.g. Fries et al., 2001). Second, by utilizing normalized FVs in the formation of distance matrices elements, *phase binding* can be tested through the Γ statistic and this actually formalizes well known techniques for the quantification of this type of inter-area interactions (e.g. Tass et al., 1998; Lachaux et al., 1999).

2.6. Association of two reconstructed trajectories

Many of the limitations of traditional linear techniques like cross-correlation or coherence-analysis can be avoided using non-linear dynamics techniques for identifying coupling between dynamical systems (Schiff et al., 1996). Dynamical interdependence in non-linear systems implies two things: either the systems communicate or they are coupled to a common driver. Originally it was sought as a

functional relation ${}^{A}X(t) = f({}^{B}X(t))$ between the dynamical variables of two systems A and B exhibiting chaotic motions (*generalized synchrony*) and the method of mutual false nearest neighbors (MFNN) was developed to test for a possible geometric connection between the trajectories in the corresponding state spaces ${}^{A}X$ & ${}^{B}X$ (Rulkov et al., 1995; Arnhold et al., 1999). The method was later advanced to incorporate characteristics like recognition of the coupling *directionality* and detection of *causal* relationships (Rulkov et al., 1995; Arnhold et al., 1999).

The key idea of the MFNN technique is that for coupled systems two close states in ${}^{A}X$ should correspond to two close states in ${}^{B}X$. A test is build by selecting for an arbitrary point ${}^{A}X(t)$ in ${}^{A}X$, the nearest State Space neighbor of this point which has time index t_{NNA}. Then as long as the trajectories are interdependent the point ${}^{B}X(t)$ in ${}^{B}X$ will have point ${}^{B}X(t_{\mathrm{NNA}})$ close neighbor. By the same token the point ${}^{A}X(t)$ will have ${}^{A}X(t_{\mathrm{NNB}})$ close neighbor, where t_{NNB} is the time index of the nearest neighbor of ${}^{B}X(t)$ in ${}^{B}X$. A ratio, known as MFNN parameter, is defined based on the corresponding four distances (see eq. 3) and used to quantify the coupling between the two systems. When only a scalar time series is available to characterize the behavior of each system, the quantification of dynamical interdependence is relied upon state-space reconstruction and delay vectors replace the state-space vectors. The MFNN parameter is a local characteristic of the reconstructed state spaces and in order to obtain reliable information about the coupling between the two systems, the statistical distribution of its values, computed at a number of state space locations, has to be studied (Rulkov et al., 1995).

Within the proposed unifying approach, the MFFN technique provides a geometric characterization of the dynamical coupling between two brain areas at a ST level. It is adapted to the visualization scheme introduced in Section 2.4 and used in a way to highlight the geometric connection between trajectories sketched on semantic maps. This enables the monitoring of brain areas coordinated behavior, using easy to understand and visualize geometrical concepts.

Given two ST time-series ${}^{A}x_{\mathrm{i}}(t)$, and ${}^{B}x_{\mathrm{i}}(t)$, the MFNN parameter is computed within the following steps. First, the 2-D reduced feature space associated with each recording site is derived. Second, the trajectory of each ST-signal is drawn on the corresponding map, using the appending technique ${}^{k}\mathrm{Y}_{\mathrm{i}}^{\mathrm{app}} = F_{\mathrm{appending}}({}^{k}\mathrm{T}_{\mathrm{i}},\ \{{}^{k}\mathrm{X}_{\mathrm{j}}\}_{\mathrm{j=1:N}}),\quad k = A,\ B$. Third, the images of the states along the drawn trajectories are used to compute the MFNN parameter

$$\mathrm{MFNN}(t) = \frac{\|{}^{B}Y_{\mathrm{i}}^{\mathrm{app}}(t) - {}^{B}Y_{\mathrm{i}}^{\mathrm{app}}(t_{\mathrm{NNA}})\|_{\mathrm{L}_2}\|{}^{A}Y_{\mathrm{i}}^{\mathrm{app}}(t) - {}^{A}Y_{\mathrm{i}}^{\mathrm{app}}(t_{\mathrm{NNB}})\|_{\mathrm{L}_2}}{\|{}^{A}Y_{\mathrm{i}}^{\mathrm{app}}(t) - {}^{A}Y_{\mathrm{i}}^{\mathrm{app}}(t_{\mathrm{NNA}})\|_{\mathrm{L}_2}\|{}^{B}Y_{\mathrm{i}}^{\mathrm{app}}(t) - {}^{B}Y_{\mathrm{i}}^{\mathrm{app}}(t_{\mathrm{NNB}})\|_{\mathrm{L}_2}} \quad (3)$$

Finally, in order to 'sketch' this parameter as a function of the location in the state-space, the (inverse) MFNN value is appended as a 3rd axis to give rise to a graph that plays the role of 'transfer function of neighborliness' between the two systems. Fig. 2 demonstrates these ideas.

3. Application to auditory M100 evoked responses

3.1. Experimental set-up

Magnetoencephalographic (MEG) data from simple auditory experiments were used to introduce the proposed framework. The whole cortex MEG-signal offered a unique environment for demonstrating the potential applications of the approach and in particular how to associate the information mined from the multichannel signal with the sources responsible for its generation.

The CTF whole head system (151 channels) was used to record MEG signals from three healthy right handed volunteers (A.F., V.P., A.O.; two males, one female; age range 25–29 years, mean 27.5). Measurements were carried out inside a magnetically shielded room with the subject sitting in a comfortable position and keeping his/her eyes open during the recordings fixating on a green spot placed 60 cm in front of the subject. The auditory stimuli were tones (1 kHz, 200 ms duration, 10 ms rise/decay time) presented in all experiments binaurally at constant inter-stimulus intervals (3 s). The loudness had been adjusted to a comfortable level for each subject, prior to the recording session (mean level: 45 dB). In each session 120 stimuli were applied. In all cases, the subject had been instructed to listen passively to the tones.

The MEG signal was recorded in continuous mode, after low-pass filtering at 208 Hz and digitization at 625 Hz. The data were further digitally band-pass filtered in the 3–100 Hz range. The continuous multichannel signal was segmented into trials lasting from −350 to 500 ms, relative to the stimulus onset. In addition, for each subject a second dataset was collected with exactly the same procedure, but with no stimulus present. This dataset, containing the STs of spontaneous brain activity, served as the record from a control condition and treated in the same manner as the record from the stimulation session.

3.2. The virtual signal (VS) transform

The analysis was focused on two signals synthesised from the multichannel data, via the VS transform, in a way to amplify the contribution from the complex of generators, at or near each auditory cortex, which are responsible for the dominant *M100* response (Makela et al., 1994). The VS transform is a data reduction technique, which computes a linear combination of signals from neighbouring channels. It usually involves the difference of two weighted sums of signals, each from one patch of sensors. A data driven method, based on the detection of the sensors showing the most prominent deflections in the averaged response, is employed for estimating the weights involved in this spatial filtering action. A detailed description of the VS construction for the study of M100 response is reported in (Liu et al., 1998). They showed that for auditory responses the VS is practically free of disturbances like occulographic or

magnetocardiographic (MCG) artifact and in addition it is a good approximation of the activation curve obtained using magnetic field tomography (MFT) (Ioannides et al., 1990) to estimate the (non-silent) current density vector from a region of interest (ROI) containing the auditory cortex.

For the results reported in the sequel, two VS were constructed, each one dedicated to one hemisphere and named, hereafter, as left VS (VS_l) and right VS (VS_r) correspondingly. Since we focused on the M100 response, which is an easily recognized early peak dominating the averaged auditory evoked magnetic field over each hemisphere, the VS were derived with the following equation:

$$VS_k(t) = \frac{1}{5}\sum_{i_k=1}^{5} S_{i_k}^{+}(t) - \frac{1}{5}\sum_{i_k=1}^{5} S_{i_k}^{-}(t), \qquad k = l,\ r \qquad (4)$$

where S_{ik}^{+} (S_{ik}^{-}) denotes the signals from sensors which were close to the corresponding auditory cortex and showed in the averaged multichannel signal the greater positive (negative) deflection in the post-stimulus period around the latency of 100 ms. In the analysis described in all the following sections, except 3.6 & 3.7, VS_l and VS_r were treated independently.

3.3. Studying the ST-sample structure via classical MDS

Classical MDS was employed to understand the geometry of the feature space corresponding to the M100 evoked response. The feature selection step was accomplished by first identifying the M100 peak in the ensemble average waveform and then delineating the M100 segment around the M100-latency via zero crossing (the mean value of dimension p, across subjects and hemispheres, was $50(\pm 3)$ and of t_1 was 62 ms). Based on the corresponding $N = 120$ ST-segments, the matrix of interpoint distances $\mathbf{D}_{[N\times N]}$ was computed and the multidimensional scaling, $\mathbf{Y}_{[N\times r]} = MDS_r(\mathbf{D})$, was applied with $r = 2$ to produce an easy to inspect image of the ST-sample structure.

The derived reduced feature space which corresponds to the ST-sample consisting of the right hemisphere evoked responses ($x(t) = VS_r(t)$) has been included in Fig. 3a, for each subject. The simplest operation to turn the depicted map to a semantic map was performed: the appending technique was used to mark the amplitude modulated versions of the average segment $\bar{X} = 1/N \sum_i X_i$, tabulated in $\mathbf{X}^{app} = [a_1\bar{X} \vdots a_2\bar{X} \vdots \ldots \vdots a_N\bar{X}]$ where a_i are scalars distributed evenly in the range $[-3\ 6]$. The axis formed in this way passes through the coordinate system origin and can provide information about the relative amplitude and timing of the peak in the ST-segments (green color denotes positive modulation, while red negative). The shown point diagrams (as well as the ones corresponding to the left hemisphere responses) reveal an anisotropy in the sample distribution that can be associated with a discrepancy in the morphological characteristics of the individual ST-patterns. The observed structure can be attributed mainly to the synchronization among *some* of the ST-segments so that their images form a 'wedge' in the reduced feature space. A few of these segments are characterized by amplitude significantly higher than the amplitude of the average segment. In addition to this structured component, the existence of spurious points can also be noticed.

The FVs extracted from the ST-sample of spontaneous activity have been appended to the previous point-diagram enabling the direct contrast (Fig. 3b) between the two recording conditions (stimulation versus rest condition) in the reduced feature space. The images of the ST-segments from spontaneous activity (red crosses) form a spherical point swarm, indicative of randomness in the phase differences between the corresponding FVs. The center of mass of this point swarm is displaced from the coordinate system origin. This displacement portrays the difference, in the averaged segment, between the two conditions and as it can be noticed it is not the most striking difference, in terms of point-distribution, between the two corresponding samples as it would be expected by the assumption of linear superimposition of a stereotypical response and ongoing activity in every trial. This contrast, of the spontaneous activity spherical point cloud with the '*wedge*' of the evoked response point sample, clearly casts doubt on *the signal-plus-noise* model and favors the hypothesis of *stimulus induced phase-reorganization* of *the brain waves* (Garrosi and Jansen, 2000; Makeig et al., 2002).

The efficiency of classical MDS in revealing signal-related structure was evaluated by utilizing the images of ST-segments in the reduced feature space to order them and employing a conventional SNR estimator (Raz et al., 1988) to quantify the signal content in the induced ST hierarchy. The ST-segment on the crest of the evoked response point sample-'wedge' was assigned the first rank [1], while the rest of ST-segments were assigned ranks [j], $j = 2{:}N$ according to the distances $\|Y_i - Y_{[1]}\|_{L_2}$. Based on the obtained *ordering list*, a sequence of SNR measurements, denoted as $SNR_{[j]}$, was computed corresponding to the sequence of subsets $\{X_i\}_{i=[1]:[j]}$, $j = 2, 3, \ldots N$; a detailed algorithmic description of how these computations were performed can be found in (Laskaris and Ioannides, 2001). These measurements revealed a progressive deterioration of SNR and therefore provided a strong evidence that the structure portrayed by the MDS maps reflects evoked response variability. In Fig. 3c the $SNR_{[j]}$ measurements have been attached to the corresponding images $Y_{[j]}$, using as a third axis the SNR value after normalization with the SNR value that corresponds to the overall set of segments, i.e. $SNR_{[j]}{}^* = SNR_{[j]}/SNR_{[N]}$. The image of the first in order segment has been denoted with a blue star. In the same way it is denoted also in Fig. 3b, where its selection can be further justified as the point lying in the neighborhood of evoked response segments that simultaneously is the farthest from the spontaneous activity point swarm.

The MDS based ordering list was exploited further for

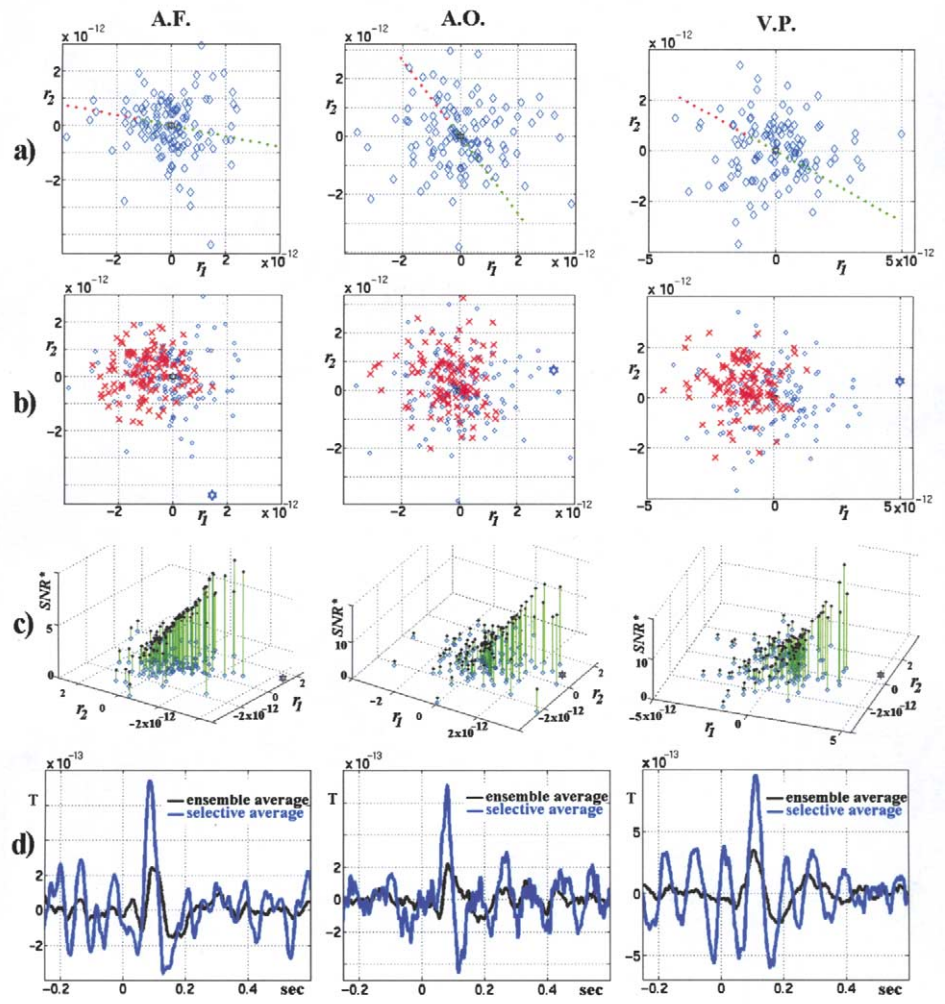

Fig. 3. Using MDS map to study the geometry of the feature space corresponding to right hemisphere M100 responses: a 'wedge is formed' by the images of the ST-segments. (a) The appended images of amplitude modulated versions of the average segment form an axis; green(red) denotes positive(negative) modulation. (b) The appended images (red crosses) of ST-segments from spontaneous activity form a spherical point cloud. (c) SNR as a function of the position of each ST-segment image relative to the ST-segment image on the crest of the formed 'wedge', which is denoted with a star. (d) Evoked response estimates produced by restricting averaging to the ten STs with the closest images to the wedge crest and by ensemble averaging.

performing *selective averaging*. By simply restricting averaging to a small portion of ST-segments on the top of the list, $\bar{X}_{\text{sel}} = 1/j_{\text{o}} \sum_{i=1}^{j_{\text{o}}} X_{[i]}$, an estimate of the M100 response was obtained in which it appeared as a deflection much sharper than in the estimate via ensemble averaging. The contrast between the selective average waveform with j_{o} only 10 and the ensemble average waveform (Fig. 3d) clearly indicates that the latter estimate suggests an underestimated amplitude scale for the evoked response, mainly because it compresses into one single waveform the time-cources of a response that is highly variable with the stimulus repetition.

3.4. Unwrapping the manifold of STs via isomap

Classical MDS is an efficient technique for producing a smooth map that can provide a sufficient global picture of the feature space geometry. Isomap (Section 2.2), on the other hand, at the expense of computational economy (due to the involved graph-theoretic steps) is capable of revealing the fine structure of the feature space by isolating from each other the distinct graph-components formed by the FVs. It can therefore result to a low-dimensional point diagram where the possible *self-organizing* tendencies in the given ST-sample stand out. A demonstrative example is given in Fig. 4, where the ST-waveforms have been configured on a plane according to the derived 2-dimensional point diagram. The morphological characteristics of the ST time-waveforms change gradually and systematically along the straight lines that emerge naturally. We refer to such lines, or ones 'drawn' on the map by controlled variation of a standard segment, as candidate *semantic geodesics* because they provide convenient pathways for navigation in the (reduced) feature space.

The ability of isomap to offer an informative *parameterization* of the ST-sample was validated by using it for the same feature space(s) where classical MDS had been applied to and following the same evaluation processes (see Section 3.3). This in turn enabled the direct comparison of the two dimensionality-reducing mappings. The matrix, $\mathbf{D}_{[N\times N]}$, of Euclidean distances was transformed to the matrix, $\mathbf{GD}^{\epsilon}$, of geodesic interpoint distances, by selecting ϵ to be equal to the average Euclidean distance and the multidimensional scaling, $\mathbf{Y} = \mathrm{MDS}_r(\mathbf{GD}^{\epsilon})$, was applied with $r = 2$. The derived point-diagram was highly structured consisting of distinct branches, i.e. semantic geodesics, converging at the center. It was easy to confirm, by visual inspection of the ST-waveforms, that the formation of distinct branches was a reflection of clustering tendencies in the sample and moreover that the order implied by the images forming each semantic geodesic followed the gradation of ST-segment morphology. In consequence the ST-segments with images residing at the tail of each branch were the most appropriate for extracting/constructing *prototypes*. The SNR measurements performed, as described in Section 3.3, for each branch separately showed that the signal content corresponding to each (important) branch was significantly higher than the signal content corresponding to the whole point-diagram. This provided an indication that isomap facilitates the efficient characterization of evoked response variability and moreover supports the delineation of prototypical responses that might contribute to the identification of the origin of this variability. The three derived point diagrams corresponding to right hemisphere evoked responses have been included in Fig. 5, in accordance with the results presented in Section 3.3 and included in Fig. 3. The most prominent branches of each point-diagram have been detected and denoted using different colors. The ST-waveforms corresponding to the images forming these branches have been grouped accordingly. The within-group averages have been computed to produce prototypical time courses of brain activity and they have been plotted using the corresponding color. The corresponding within-group SNR measurements have been attached to these curves, after normalization with the SNR measurement for the overall set. Along with each one of these *subaverages*, the ensemble average has been plotted (in black) for a direct contrast. These graphs clearly suggest that the phase (peak-timing) of the ST-segments is an important dimension of variation in the evoked response.

In addition, they provide a strong hint that the evoked response depends on the status of prestimulus activity

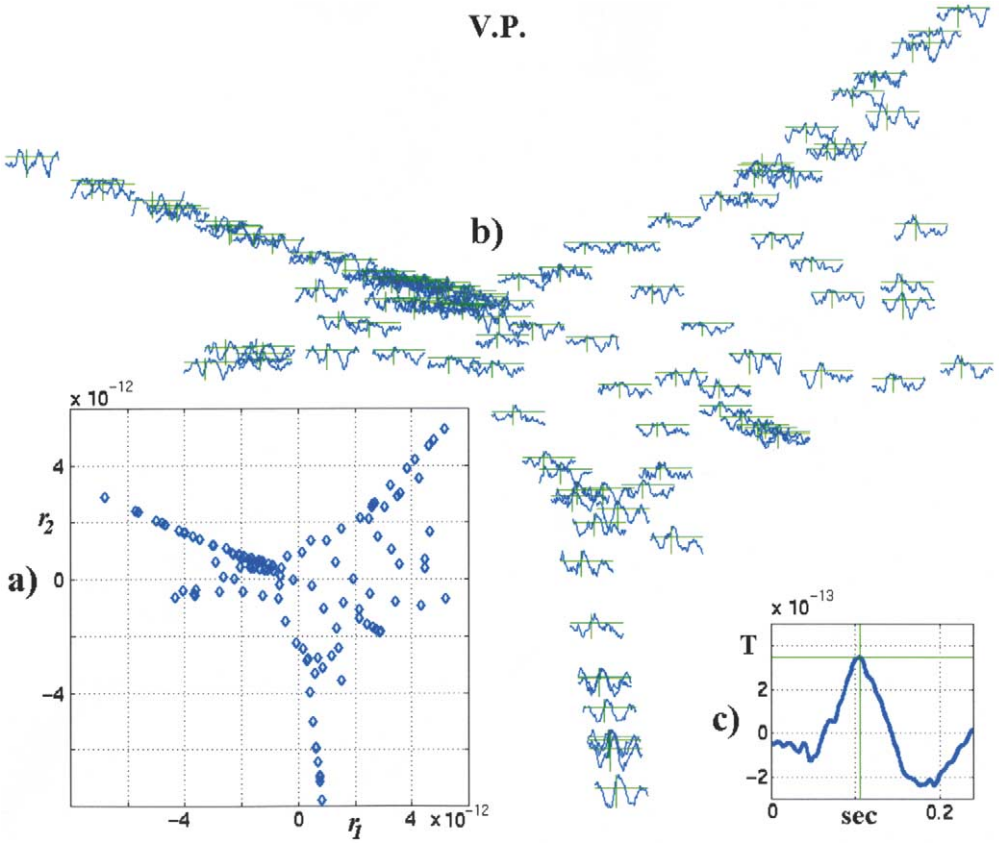

Fig. 4. (a) Isomap based reduced feature space corresponding to right hemisphere M100 responses of subject V.P. (b) The ST time-waveforms have been configured on a plane according to the reduced feature space coordinates of their images. All the waveforms share a common time/amplitude scale, while the vertical (horizontal) green line indicates the latency (amplitude) of the M100 peak in the ensemble average of the STs. (c) The ensemble average waveform.

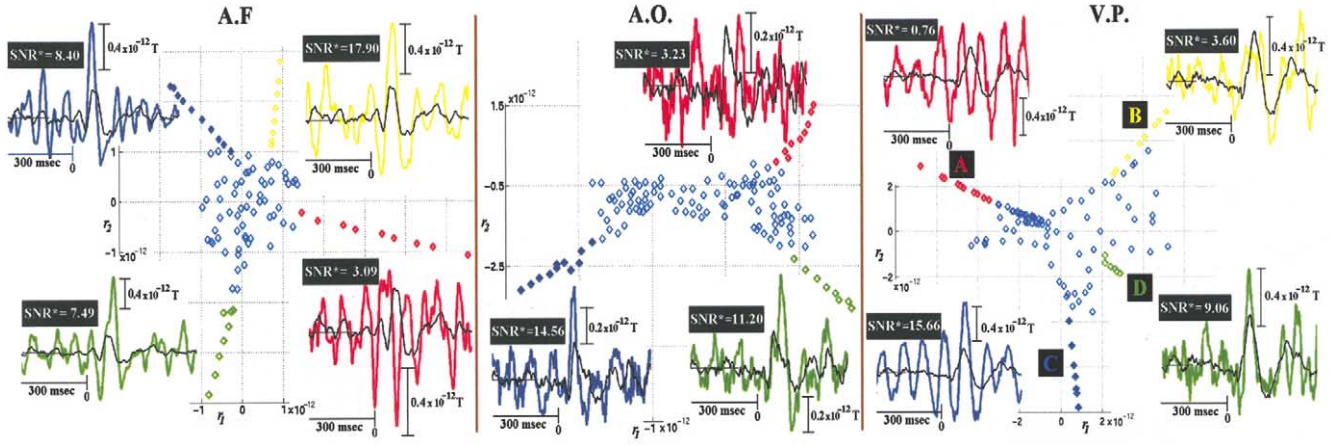

Fig. 5. Using isomap to unfold the manifold of the ST-sample which contains the right hemisphere M100 responses. The most prominent branches of this point-diagram were detected (painted in a different color) and the ST-waveforms corresponding to the images forming these branches were grouped accordingly and averaged to produce four prototypical time courses of brain activity. The prototypes have been plotted (using the corresponding colors) along with the ensemble average waveform (black curve).

(Makeig et al., 2002), since the extracted prototypical time courses are not dissimilar only in the latency-range where the grouping was based on (i.e. the ST-segments latencies), but also well before the stimulus onset. The comparison of the subaverages plotted (intentionally) in blue with the corresponding selective averages given in Fig. 3 shows that the results from the analysis based on isomap do not contradict the results from the analysis based on classical MDS. Isomap, by unraveling the original ST-manifold on a plane, provides a more detailed image of the ST-sample structure.

The isomap based characterization of evoked response variability provides hints for the origin of this variability, which we explore briefly through source reconstruction of the data from each of the four prototypes for subject V.P. (Fig. 5). Among the four prototypes (A–D), only prototype D (green curve) is clearly fully compatible with the time course of activity portrayed by the ensemble average (black curve). Prototype C (blue curve) is characterized by increased amplitude and persistent oscillatory activity throughout the whole time range. Prototype B (yellow curve) hardly portrays evoked response, while prototype A (red curve) has no obvious evoked response at the peak latency of the average segment. We applied MFT, after the multichannel ST-data had been grouped and averaged accordingly, in order to explore the spatial distribution of

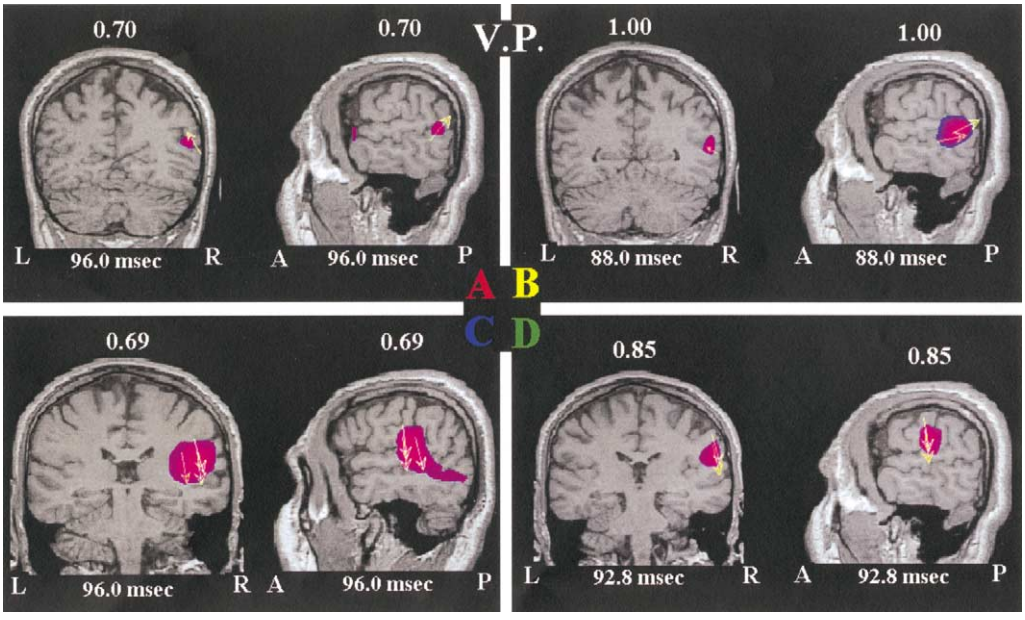

Fig. 6. MFT based maps of the different brain activity modes associated with the four prototypes given in Fig. 5 for subject V.P. Each one of the four maps portrays the instantaneous current source density distribution at the post-stimulus time instant of maximum current intensity.

activity and hence the neural circuitry responsible for the generation of these prototypes. A series of maps representing the MFT estimates of brain activity, on a millisecond by millisecond basis, were computed from the MEG data corresponding to each prototype. We are describing here, only the activity at the poststimulus time instances, close to the peak latency of the average segment, where the MFT resulted in the strongest activity estimates. This description is restricted to the immediate neighborhood of the area that the VS transform was designed to be sensitive at. The four instantaneous maps of current source density distribution are shown in Fig. 6. To ease comparison the current density in the four maps, which originally were normalized independently, has been printed as a fraction of the overall maximum (in map B). The identification of focal activity in the right auditory cortex proper with maximum latency of 93 ms is evident in the prototype D map, while a rather more extended activity is seen in the case of prototype C map with maximum 3 ms later. In the case of prototypes A and B, the activity is identified in a more posterior parietal area. These cursory remarks are made just to highlight some of the features of the MFT solutions. A proper analysis of the content of these maps requires exploration of the spatiotemporal variation of the current density across the brain, and it is beyond the scope of this work.

3.5. Qualitative study of the evoked response dynamics

The traditional pattern analysis approach for characterizing an evoked response is based solely on the extracted FV. In terms of our geometrical consideration this characterization is equivalent to the identification of the neighborhood where the certain FV lies, given that the study of the feature space topology has been preceded. On the other hand, nonlinear time series analysis offers the perspective of characterizing the dynamics of a response by taking into account the evolution of brain activity from prestimulus status to poststimulus reaction (Jansen et al., 1994). The marriage of the two techniques, introduced in Section 2.4, combines in one what is lost in each signal-analysis approach.

The trial-to-trial variability, for each ST-sample, was studied in dynamical terms in the MDS-based reduced feature space, which had been previously employed for understanding the global sample-geometry. Using the appending technique the trajectories reconstructed from the (single-trial/subaveraged/averaged) evoked responses were visualized as 2-dimensional semantic orbits.

The orbit from the ensemble average signal and the orbits from STs were markedly different. The ensemble average showed a dynamical system at rest in the pre-stimulus period which was 'kicked-out' by the arrival of the stimulus in a transient excursion, before returning to quiescence in the far post-stimulus period. In contrast, the ST-orbits represented a continuously active non-linear system. A characteristic example of this contrast can be seen in Fig. 7, where the trajectories reconstructed from the average signal (top) and from four STs (bottom) of the same record, from subject V.P., have been sketched on the same semantic map (initially shown in Fig. 3). It is evident that the M100 component seen, as a clear deflection, in the average response cannot be attributed, simply, to an abrupt increase of activity from a zero baseline occurring in a stereotyped manner in every trial.

The comparison between the orbits corresponding to the different prototypical responses, which had been delineated via the isomap-based analysis, revealed distinct dynamic regimes. It was verified that each prototypical orbit was consistent with the dynamics of the individual ST responses included in the corresponding group. This study showed that ongoing activity is coupled with the response and more specifically provided evidence for the dependence of response on the prestimulus dynamics (Jansen et al., 1994; Ioannides et al., 1998). A typical example of the different patterns of dynamics that can be mined from a ST-sample is given in Fig. 7. The middle panel includes the four different orbits corresponding to the prototypical responses shown in the Fig. 5 for subject V.P. The bottom panel includes orbits from STs that have been selected randomly from the corresponding groups. The fragments of each orbit have been plotted using red, blue and green color to indicate accordingly the time range of (−320, 0), (0, 200) and (200, 550) ms. Only the orbits B and D indicate stimulus induced transient dynamics. They both depict an excursion from the prestimulus attractor, but towards opposite directions. Taken into account the known topology of the feature space (from Fig. 3), this *bifurcation* might indicate the existence of counterbalancing forces controlling the motion during the response (i.e. excitatory/inhibitory circuitry). Both orbits A and C correspond to deterministic non-linear oscillators in unperturbed motion. However, considering the semantics of the map, the former oscillator appears indifferent to, while the latter oscillator entrained to the applied periodic forcing (i.e. the auditory stimulation every 3 s).

3.6. Interhemispheric binding: the structural association approach

Assuming proper feature selection, the emerged structure in the feature space is a reflection of the trial-to-trial variability. Inter-area association, in the sense of functional covariation over stimulus repetition (Friston et al., 1997; Lachaux et al., 1999; Fries et al., 2001), can therefore be sought as structural correspondence between the feature-spaces constructed from signals such each one represents the activity in a distinct brain area. Hubert's test is a suitable one for assessing the statistical significance of such correspondence. It is computationally compatible with the derivation of semantic maps and therefore it can be used symbiotically with them. The application of this test should follow the study of feature space geometry that can confirm the appropriateness of the feature selection step and the purity of the data from singularities (like artifact contami-

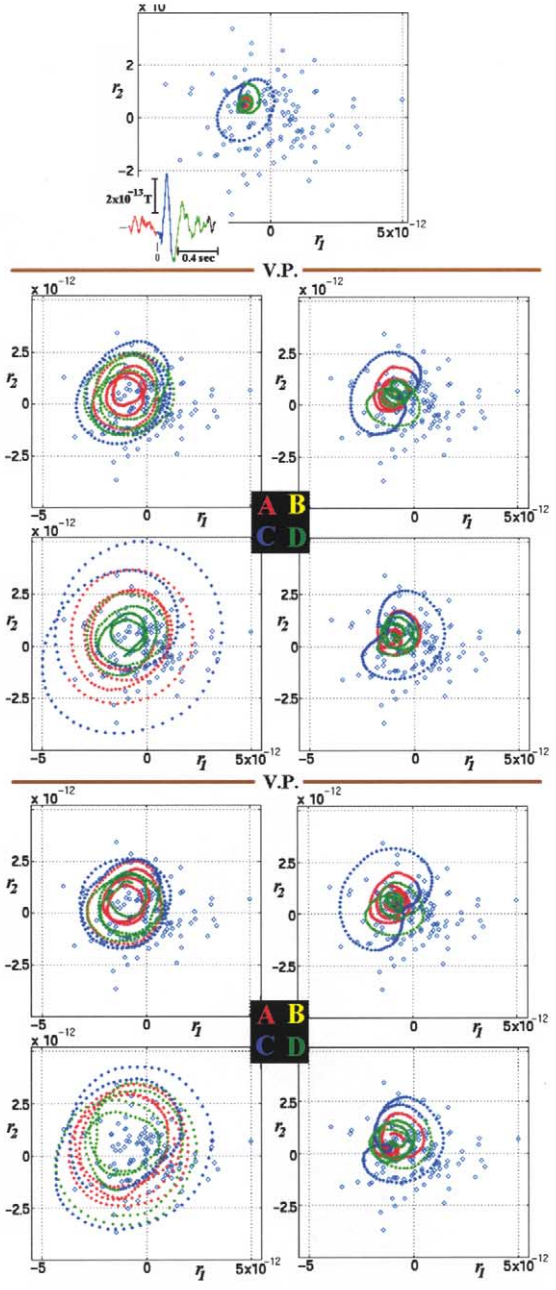

Fig. 7. Contrast of qualitative dynamics extracted from the average response (top) with the dynamics corresponding to the four prototypical responses defined in Fig. 5 for subject V.P. Middle/bottom panel contains the orbits from the subaverages/individual STs. Red/blue/green fragment correspond to (−320, 0 ms)/(0, 200 ms)/(200–550 ms) signal timerange.

nation that might lead to equivocal results). Hubert's test can also be used for ranking putative functional covariation scenarios, as it is shown next, for probing functional connectivity between left and right auditory cortices.

Three different covariation scenarios were tested using first the broadband signal, and then filtered signal in specific frequency ranges. The three alternatives were *segment covariation*, *amplitude covariation* and *latency covariation*. It should be noticed that the first scenario 'contains' the other two. Functional connectivity was tested both for the ST-samples of evoked responses and for the ST-data from the control recording condition.

In all three cases, the feature extraction step was guided by the average M100 segment and performed independently for each one of the two time series ${}^{l}x(t) = \mathrm{VS_l}(t)$ and ${}^{r}x(t) = \mathrm{VS_r}(t)$ leading to the data-matrices ${}^{l}\mathbf{X}$ and ${}^{r}\mathbf{X}$ with the i-th row containing the ST-segment

$$ {}^{k}X_i = [{}^{k}x_i[{}^{k}t_1],\ {}^{k}x_i[{}^{k}t_1 + T_s],\ {}^{k}x_i[{}^{k}t_1 + 2\times T_s],\ \ldots,\ {}^{k}x_i[{}^{k}t_1 + ({}^{k}p - 1)\times T_s]], \qquad i = 1:120, \qquad k = l,\ r. $$

In the case of *segment covariation*, the distance matrices, ${}^{l}\mathbf{D}$ and ${}^{r}\mathbf{D}$, were computed directly from the corresponding data-matrices and the application of Hubert's test quantified the statistical significance of the match between the point-sample structures. The results were expressed in terms of probability that the rows of ${}^{r}\mathbf{X}$ had been inserted at random relative to the rows of ${}^{l}\mathbf{X}$. In the case of *amplitude covariation* the distance matrices were computed from the two matrices ${}^{l}\mathbf{X}'$ and ${}^{r}\mathbf{X}'$ containing (as 1-dimensional FVs) the lengths of the corresponding vectors, i.e.

$$ {}^{k}\mathbf{X}'_{[N\times 1]} = [\|{}^{k}X_1\|_{L_2} \vdots \|{}^{k}X_2\|_{L_2} \vdots \ldots \vdots \|{}^{k}X_N\|_{L_2}], \qquad k = l,\ r. $$

After noting that $\|{}^{k}X_i\|_{L_2}$ equals $({}^{k}p)^{1/2}$ times the RMS value of the corresponding ST-segment, it is easily deduced that this single feature described the amplitude variation over trials and therefore the application of Hubert's test quantified the amplitude covariation of the left and right auditory responses

In the case of *latency covariation* the distance matrices were computed, after the normalization of the FVs, from the two matrices ${}^{l}\mathbf{X}^*$ and ${}^{r}\mathbf{X}^*$

$$ {}^{k}\mathbf{X}^* = [{}^{k}X_1/\|{}^{k}X_1\|_{L_2} \vdots {}^{k}X_2/\|{}^{k}X_2\|_{L_2} \vdots \ldots \vdots {}^{k}X_N/\|{}^{k}X_N\|_{L_2}], \qquad k = l,\ r. $$

The subsequent application of Hubert's test expressed the latency covariation between the left and right hemisphere evoked responses, since the Euclidean distance between two normalized ST-segments expresses their (inverse) synchronization, so that the structure in each feature space arises primarily from the relative timing differences of the ST-responses (Laskaris and Ioannides, 2001).

The three alternatives were tested also after filtering (using 3rd-order Butterworth-type filters in a zero-phase distortion mode) the two time series ${}^{l}x(t)$ and ${}^{r}x(t)$ in the frequency ranges: 4–8, 8–12, 12–16, 16–30 and 30–100 Hz. Despite the fact that the filtered versions, denoted as ${}^{l}\chi(t)$ and ${}^{r}\chi(t)$, were used in the succeeding feature-extraction step, the ST-segment latency ranges were kept as in the case of broadband signals, i.e. the rows of the data-matrices ${}^{l}\mathbf{X}$ and ${}^{r}\mathbf{X}$ took the following form

$$ {}^{k}X_i = [{}^{k}\chi_i[{}^{k}t_1],\ {}^{k}\chi_i[{}^{k}t_1 + T_s],\ {}^{k}\chi_i[{}^{k}t_1 + 2\times T_s],\ \ldots,\ {}^{k}\chi_i[{}^{k}t_1 $$

Table 1
Hubert's test quantifying the functional covariation between the left and right auditory cortex

Γ (*P* value)[a]		Segment (broadband)	Amplitude (broadband)	Phase (4–8 Hz)
A.F.	Evoked response	5.438 (5.3×10^{-8})	1.085 (0.278)	2.852 (0.004)
	Spontaneous activity	1.359 (0.174)	1.556 (0.119)	1.047 (0.295)
A.O.	Evoked response	3.972 (7.1×10^{-5})	1.051 (0.293)	3.635 (2.8×10^{-4})
	Spontaneous activity	0.073 (0.941)	− 0.302 (0.763)	1.493 (0.135)
V.P.	Evoked response	1.611 (0.107)	− 0.075 (0.940)	1.389 (0.165)
	Spontaneous activity	1.329 (0.184)	1.533 (0.125)	0.284 (0.7765)

[a] *P* value expresses the probability that the order of the responses recorded from the right hemisphere is independent of the order of the responses recorded from the left hemisphere.

$+({}^{k}p - 1) \times T_s]]$, $i = 1 : 120$ & $k = l,\ r$.

In the case of normalized ST-segments the Euclidean distances, computed after the band pass filtering, express the phase differences between the corresponding (filtered)-segments, and therefore the test for latency-covariation scenario becomes a means of detecting phase synchrony in the evoked activity, within the selected frequency band, of the two cortices.

In summary, the contrast between the results from the two recording conditions (evoked response versus spontaneous activity) clearly showed that the stimulus is responsible for a functional covariation between the two auditory cortices. The latency-covariation scenario fitted our experimental data much better than the amplitude-covariation one. The segment-covariation scenario offered a slight improvement on the former scenario. The comparison between the selected frequency channels, regarding all three types of covariation, showed that the (4–8 Hz) band has by far the most important contribution to the observed stimulus-induced functional coupling of right and left auditory cortices. Specifically, our results supported strongly the hypothesis of inter-hemispheric phase binding. Table 1 includes the most important among the results from the application of Hubert's test to the ST-data from all three subjects. From the tabulated *P*-values, the importance of (4–8 Hz) phase binding in the detected brain synchrony becomes evident.

3.7. Interhemispheric binding: the dynamical interdependence approach

The pattern analysis approach (adopted in the previous section) enables the detection of functional connectivity by identifying the structural association between feature spaces. It exploits the trial-to-trial variability of the evoked response and hence probes the interdependence between brain areas at a *relative large time scale*, controlled by the inter-stimulus interval. Such a characterization is general and it applies to the overall ST-sample. The use of non-linear dynamics approach (Section 2.6) for detecting the structural association between reconstructed evoked response trajectories enables the identification of interdependence at a *fast time scale* and hence provides a characterization of the interareal coupling at the level of individual trials. This might be proved useful for experimental settings where the strength of coupling is changeable during the recording session (e.g. due to the induced learning). In the sequel we are presenting the results from the application of the MFNN technique to the pair of VSs for detecting possible dynamical coupling between the two hemispheres.

The steps, described in Section 2.6, were employed using the ST time series of the VSs, i.e. ${}^{A}x_i(t) = {}^{l}x_i(t)$ and ${}^{B}x_i(t) = {}^{r}x_i(t)$, and the MFNN parameter was computed, on a millisecond by millisecond basis, with the formula of eq. 3. The same steps were repeated for estimating this parameter for the ST time series corresponding to the control recording condition. In the latter case the trajectories of spontaneous activity were drawn on the semantic map from the ST-data corresponding to the stimulation session.

The results are shown in Fig. 8, one column for each subject. The first two rows show the inverse of the MFNN parameter represented by a gray-scale code with the white-grade corresponding to 1 and denoting maximal interdependence (color-coding, due to the sporadic character of the measurements, should be adjusted separately for each subject/condition in order to provide an efficient visualization and was avoided). The first(second) row shows the results for the control (active) condition respectively, enabling the direct visual contrast of the functional coupling of the two auditory cortices between these two conditions. The stimulus related increase in the estimated generalized synchrony is evident. The displays highlight apart from the intra-trial variability, also the non-stationary character of the dynamical coupling even along the timerange of individual trials, suggesting that the observed coupling is served by fast transient events.

To obtain a *coarse* picture for the timecourse of coupling, the previous (inverted) MFNN measurements have been averaged across trials and the resulting timecourse is shown in the third row of Fig. 8. The stimulus-

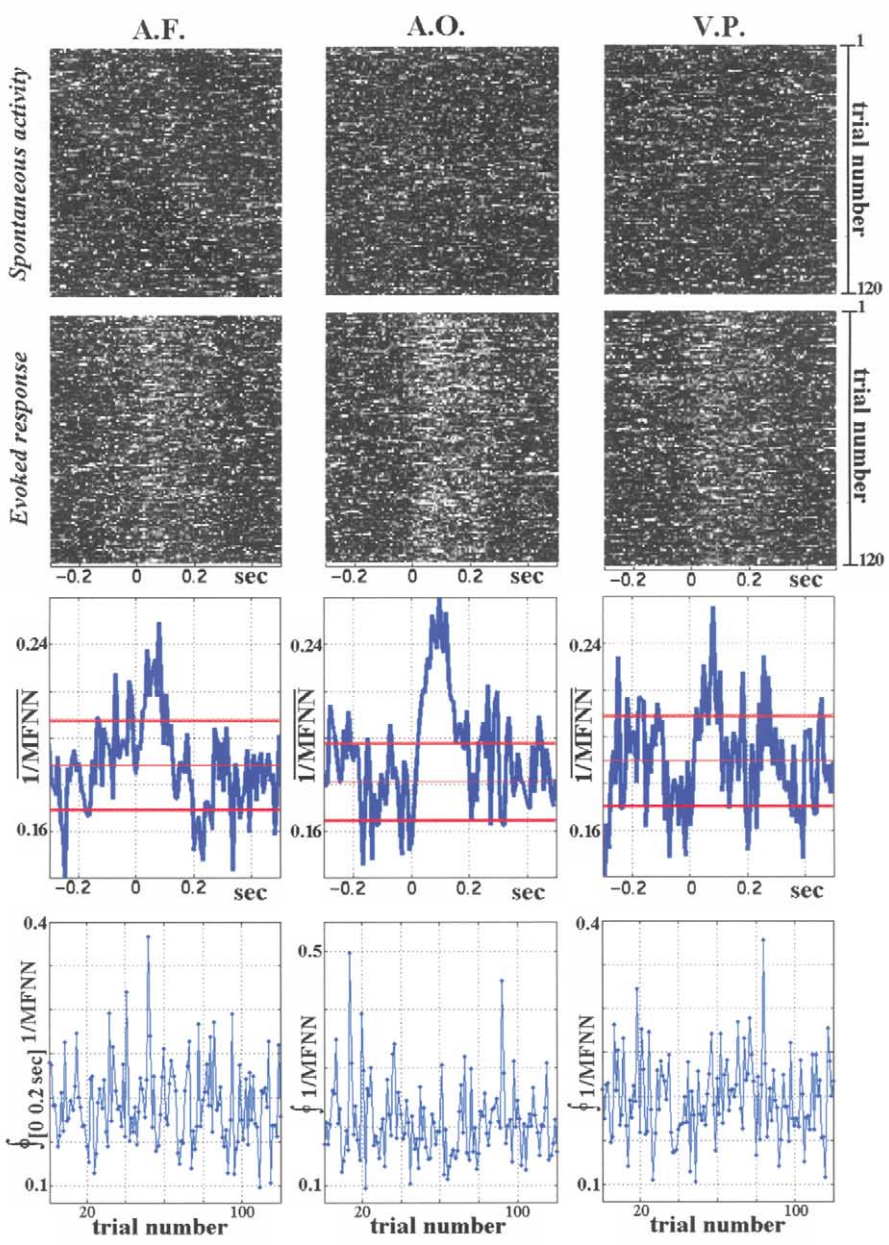

Fig. 8. Quantifying inter-hemispheric binding, as dynamical interdependence, using the MFNN parameter.

induced increase in the dynamical coupling is evident. To rule out the possibility that this increase was simply a byproduct of the simultaneous excitation (due to the binaural stimulation) of both auditory cortices, the common practice of *data shuffling* was followed. The order of the right VS-STs was randomized and the previous computations were repeated. The average (across trials) of the inverted MFNN measurements was estimated for 200 repetitions of the shuffling procedure. The mean value and the standard deviation of these 200 waveforms were computed. The red horizontal lines in the graphs of third row of Fig. 8 show the mean-value as a thin line and the mean-value plus (minus) two times the standard deviation as the upper (lower) thick line. A statistically significant stimulus-induced increase in the dynamical coupling of the left and right auditory cortices remains above the later line soon after stimulus onset.

To obtain a *coarse* picture for the timecourse of coupling along the trial-to-trial dimension, the (inverted) $MFNN_i(t)$ measurements have been averaged in the (0, 0.2 s) time-range, within each trial separately, and plotted as a function of stimulus repetition number in the last row of Fig. 8. Surprisingly, the obtained waveform indicates the existence of a complex process responsible for controlling the

observed dynamical coupling which is characterized by both medium (corresponding to the stimulus repetition rate) and long (corresponding to the timerange of, approximately, ten trials) time scales.

4. Discussion

In this paper a unifying ST-analysis methodology was introduced, bringing together principles from pattern analysis and non-linear dynamics. Pattern analysis tools provide the geometrical perspective necessary to explore the multidimensional space defined by ST-patterns. The introduction of algorithmic techniques from non-linear dynamics allow a description of evoked responses as trajectories in this well-defined geometrical framework. The feature-vector extracted from a ST-pattern emerges as a snapshot of the response generation process dynamics. The study of structure and dynamics of a ST-sample is therefore unified, and it is reduced to the understanding of the feature space geometry. Semantic maps serve this understanding because their core geometric properties, i.e. points, lines and regions, correspond respectively to meaningful prototypes, parameterizations and states. Semantic maps are a low dimensional space representation arrived via MDS and as such they provide meaningful visualization of both the structure and dynamics in the form of point-diagrams and orbits in a low dimensional space that is easy for the human eye to analyze. The approach lends itself equally well to the study of individual ST-samples, and the comparison of different samples of STs representing the evoked activity from two or more distinct brain areas. Functional connectivity is defined by the geometrical similarity between the corresponding point-diagrams, while dynamical interdependence as degree of geometrical association between the corresponding orbits. Well-established tests from multivariate statistics and non-linear dynamics, accordingly, have been adapted to quantify the significance of these associations. The overall approach has a unifying character also regarding computations. Using a common algorithmic substratum: a ST-sample of brain activity patterns can be described in structural terms, patterns of dynamical behavior characterizing a brain area can be sketched and patterns of dynamical interactions between brain areas can be derived. The inherent vectorial nature of the algorithmic procedures allows preprocessing with existing methodologies for artifact elimination (e.g. Laskaris et al., 1997) and noise suppression (e.g. Effern et al., 2000) and post-processing by most of the Pattern Analysis techniques, cited herein, for passing from a qualitative description to the quantitative modeling of the process generating the ST-data.

The geometrical tools for ST-analysis, used within the introduced framework, includes: classical MDS-map for obtaining a global picture of the sample-structure and sketching the ST-trajectories, isomap for extracting prototypical modes of response, Hubert's test for detecting functional covariation and MFNN-technique for detecting dynamical coupling. We have shown that a rich interplay is possible between the items in this condensed list and we have demonstrated through applications to real data its effectiveness. Specifically, we have used magnetoencephalographic data from a simple auditory paradigm. The emphasis was placed on validating and testing the usefulness of the cardinal concept of our work, namely semantic maps. The results confirm that the semantic maps can deepen our understanding of the response generation process, but they go beyond a simple justification of the method. Some of the results constitute vivid confirmation of well-known hypotheses while others lead to new insights deserving further study.

A reliable characterization of the trial-to-trial variability was achieved showing the coupling of ongoing activity and evoked response. Prototypical time courses of activity were extracted and proved to provide meaningful abstractions of the underlying process along a wide timerange, from far prestimulus to poststimulus intervals. Specifically the isomap analysis was applied to the ST time series representing estimates of the activity from a well circumscribed brain region within a well defined latency-range. The distinct response classes that emerged described activity from wider brain regions and extended latency ranges. Figs. 5–7 show that the spatial and temporal facets of evoked response variability can be represented in an organized and intelligible way. This representation points out that the variability seen in the recorded signal very likely results from the way distinct cortical substructures are engaged in the response generation (Makeig et al., 2002). A similar approach has been used to identify response classes in a somatosensory stimulation paradigm (Ioannides et al., 2002). The extracted prototypical activation-curves from a ROI containing the secondary sensory areas SII led to the identification of distinct communication modes between primary sensory area (SI) and SII.

Functional covariation between the left and right hemisphere responses was detected in the form of stimulus induced phase-locking in the (4–8 Hz) range. Fast interactions between the two cortices were also detected and shown to be modulated by a non-linear mechanism operating at longer time scales. The mosaic of all individual results revealed a complex spatially-extended dynamical system with the tendency of self-organization not only in response to external stimuli, but also to internally-triggered events.

The restriction of analysis to (sub)averaged data, specific frequency channels, certain signal features or latency-ranges and single recording sites, though necessary in practice, may hide important evoked events and therefore should be carefully designed. The approach advocated here is *empirical* in nature and provides a direct processing path leading from the collected data to the essence of evoked response, guided by the intrinsic nature of the data. An approach similar in spirit to ours has been employed previously, in animal studies, for contrasting spatial patterns of activity in response to conditioned stimuli (Barrie et al., 1999).

In conclusion we have demonstrated that human brain's function must be seen as a process with history, even when responses to simple identical stimuli are studied. Furthermore, we have shown that the systematic study of order behind the fluctuating activity in single trials is possible using non-invasive measurements.

Acknowledgements

One of the authors (N.A.L) is deeply indebted to S. Fotopoulos for the priceless introduction to the vectorial processing of multidimensional signals and to P. Ktonas for previous invaluable discussions.

Appendix A. Classical (metric) MDS

Given the matrix of inter-point distances $\mathbf{D}_{[N\times N]}$ characterizing a sample of N points $\{P_i\}_{i=1:N}$ in R^P, MDS provides a projection of the sample in a low dimensional space via the following operations applied to **D**.I. Elementwise squaring: The matrix $\mathbf{S}_{[N\times N]}$ with elements $S(i,\ j) = D(i,\ j)^2$ is computed. **S** can be computed directly from the data-matrix $\mathbf{X}_{[N\times p]}$.

$$S = \mathrm{diag}(\mathbf{A})\mathbf{E} + \mathbf{E}\,\mathrm{diag}(\mathbf{A}) - 2\mathbf{A},$$

where $\mathbf{A} = \mathbf{X}\mathbf{X}^{\mathbf{T}}$ & $\mathbf{E}_{[N\times N]} : E(i,\ j) = 1$

II. Centering: the centering operator $\mathbf{H}_{[N\times N]}$, $H(i,\ j) = \delta_{ij} - 1/N$ is applied to **S**

$$\mathbf{B} = -\mathbf{HSH}/2$$

III. *Eigenvector* analysis: the p ($p \le N - 1$) non-zero eigenvalues of **B** λ_i, $i = 1{:}p$ are identified (in decreasing order) and the corresponding eigenvectors are standardized so as $Z_i \cdot Z_i^{\mathrm{T}} = \lambda_i$ and tabulated in

$$\mathbf{Z}_{[N\times p]} = [Z_1 \vdots Z_2 \vdots \ldots \vdots Z_p]^{\mathrm{T}}$$

IV. The image of P_i in the space of reduced dimensions r is given by the vector Y_i with coordinates the r first elements of the ith row in **Z**, i.e. $\mathbf{Y}_{[N\times r]} = \mathrm{MDS}_r(\mathbf{D}) = \mathbf{Z}(:,\ 1{:}r)$.

Appendix B. Isomap

Isomap is an extension of classical MDS that includes a transformation of the original distance matrix $\mathbf{D}_{[N\times N]}$ to the matrix $\mathbf{GD} = \mathbf{G}(\mathbf{D})$ that contains the shortest path distance between all pair of points:I. A weighted graph G is defined over all N points by connecting points P_i & P_j if (as measured by $D(i, j)$) they are closer than ϵ. The corresponding edge weights are initialized to $GD(i, j) = D(i, j)$ if P_i, P_j are linked by an edge; $GD(i, j) = \infty$ otherwise.II. For each $k = 1, 2, \ldots N$ in turn, all entries $GD(i, j)$ are replaced by $\min\{GD(i, j),\ GD(i, k) + GD(j, k)\}$. The fraction of points not connected to the main component of the resulting graph is detected and deleted from further analysis. As ϵ is reduced more points are deleted.III. The images Y_i of points P_i in a space of reduced dimensions r are derived via the application of classical MDS, $\mathbf{Y}_{[N'\times r]} = \mathrm{MDS}_r(\mathbf{GD})$.

Appendix C. Appending technique

Let a point set $\{P_i\}_{i=1:N}$ in R^p, with data-matrix $\mathbf{X}_{[N\times p]}$, that has already been projected to the vector set $\mathbf{Y}_{[\mathbf{N\times r}]}$ using classical MDS. Given a point set $\{P_j^{\mathrm{app}}\}_{j=1:N2}$ in R^p, with data-matrix $\mathbf{X}^{\mathrm{app}}$, an efficient way to add their images in the predefined *r-D* space is accomplished within the following steps, which constitute extension of a previous method (Gower, 1968):I. The inter-set distances are first computed, in R^p, and tabulated in **W**: $W(i, j) = \|X_i - X_j^{\mathrm{app}}\|_{L2}$.

$$\mathbf{W}_{[N\times N_2]} = \mathrm{diag}(\mathbf{X}\mathbf{X}^{\mathbf{T}})\hat{1}_{[1\times N_2]} + \hat{1}_{[N\times 1]}(\mathrm{diag}(\mathbf{X}^{\mathbf{app}}(\mathbf{X}^{\mathbf{app}})^T))^{\mathrm{T}}$$

$$-2\mathbf{X}(\mathbf{X}^{\mathbf{app}})^T, \qquad \hat{1} = [1,\ \ldots\ ,\ 1]$$

II. Then the coordinates of P_j^{app} images are estimated, using

$$\mathbf{Y}^{\mathrm{app}}_{[N_2\times r]} = \tfrac{1}{2}((\mathbf{Y}^T\mathbf{Y})^{-1}Y^T\,\mathrm{d}\mathbf{W})^{\mathrm{T}}, \qquad \mathrm{d}\mathbf{W}_{[N\times N_2]} = \mathrm{diag}(\mathbf{B})\hat{1}_{[1\times N_2]} - \mathbf{W}$$

where the matrix **B** has been defined in Appendix A.

If the pre-estimated projection has been produced via the Isomap technique, the above technique can easily be adapted so as to align with the notion of 'neighboringless', by restricting the preservation of geometrical relationships to the ones between each point to be appended and the points in $\{P_i\}_{i=1:N}$ which are less distant than ϵ.

Appendix D. Hubert's Γ statistic

Given two proximity matrices ${}^{\mathbf{A}}\boldsymbol{\Delta}_{[\mathbf{N\times N}]}$ and ${}^{\mathbf{B}}\boldsymbol{\Delta}_{[\mathbf{N\times N}]}$, the normalized form of Hubert's Γ is:

$$\Gamma_n = \frac{2}{N(N-1)^{\mathrm{A}}s^{\mathrm{B}}s}\sum_{i=1}^{N-1}\sum_{j=i+1}^{N}[{}^{\mathrm{A}}\Delta_{(i,j)} - {}^{\mathrm{A}}m][{}^{\mathrm{B}}\Delta_{(i,j)} - {}^{\mathrm{B}}m]$$

Where ${}^{\mathrm{A}}m({}^{\mathrm{B}}m)$, ${}^{\mathrm{A}}s({}^{\mathrm{B}}s)$ denote respectively the mean value and the standard deviation of the proximity matrix ${}^{\mathbf{A}}\boldsymbol{\Delta}$ (${}^{\mathbf{B}}\boldsymbol{\Delta}$) entries. The *random label hypothesis* is stated as follows:$\mathbf{H_o}$: All permutations of the row (and column) labels of ${}^{\mathbf{A}}\boldsymbol{\Delta}$ are equally likely. The permutation corresponds to a reordering of the labels $\{1, 2, \ldots N\}$. The distribution of Γ_n under H_o must be estimated (feasible for $N < 8$) or approximated to fix a threshold and establish how large is 'large'. The latter can be achieved via Monte Carlo analysis. As an alternative way of assessing whether Γ_n is significantly large, they have suggested 'under the assumption that the underlying distribution is normal' the use of the following normalized statistic

$$\Gamma^* = [\Gamma_n - E(\Gamma_n)]/s(\Gamma_n)$$

where $E(\Gamma_n)$ and $s(\Gamma_n)$ are the mean and standard deviation of the Γ_n that can be computed with closed formulas from the

entries of both proximity matrices (Hubert and Schultz, 1976).

References

Abarbanel HDI. Analysis of observed chaotic data, 134. New York: Springer, 1996. pp. 419–430.

Arieli A, Sterkin A, Grinvald A, Aertsen Ad. Dynamics of ongoing activity: explanation of the large variability in evoked cortical responses. Science 1996;273:1868–1871.

Arnhold J, Grassberger P, Lehnertz K, Elger CE. A robust method for detecting interdependences: application to intracranially recorded EEG. Physica D 1999;134:419–430.

Barrie JM, Holcman D, Freeman WJ. Statistical evaluation of clusters derived by non-linear mapping of EEG spatial patterns. J Neurosci Methods 1999;90:87–95.

Burioka N, Cornelissen G, Halberg F, Kaplan D. Relationships between correlation dimension and indices of linear analysis in both respiratory movement and electroencephalogram. Clin Neurophysiol 2001;112:1147–1153.

Donchin A, Heffley E. Multivariate analysis of event-related potential data: a tutorial review. In: Otto D, editor. Multidisciplinary perspectives in event-related brain potential research, Washington, DC: Government Printing Office, 1978.

Effern A, Lehnertz K, Fernandez G, Grunwald T, David P, Elger CE. Single trial analysis of event related potentials: non-linear de-noising with wavelets. Clin Neurophysiol 2000;111:2255–2263.

Fries P, Neuenschwander S, Engel AK, Goebel R, Singer W. Rapid feature selective neuronal synchronization through correlated latency shifting. Nat Neurosci 2001;4(2):194–200.

Friston K, Stephan K, Frachowiak R. Transient phase-locking and dynamic correlations: are they the same thing? Hum Brain Mapp 1997;5:48–57.

Garrosi V, Jansen B. Development and evaluation of the piecewise Prony method for evoked potential analysis. IEEE Trans Biomed Eng 2000;47(12):1549–1554.

Gath I, Bar-On Eh, Lehmann D. Automatic classification of visual evoked responses. Comput Methods Prog Biomed 1985;20:17–22.

Geva A. Feature extraction and state identification in biomedical signals using hierarchical fuzzy clustering. Med Biol Eng Comput 1998;36:608–614.

Geva A, Pratt H. Unsupervised clustering of evoked potentials by waveform. Med Biol Eng Comput 1994;32:543–550.

Gower JC. Adding a point to vector diagrams in multivariate analysis. Biometrika 1968;55:582–585.

Gray CM. The temporal correlation hypothesis of visual feature integration: still alive and well. Neuron 1999;24:31–47.

Hoppe U, Weiss S, Inbar G. Overcoming selective ensemble averaging: unsupervised identification of event-related brain potentials. IEEE Trans Biomed Eng 2000;47:822–826.

Hubert L, Schultz J. Quadratic assignment as a general data analysis strategy. Br J Math Statist Psychol 1976;29:190–241.

Ioannides A, Bolton J, Clarke C. Continuous probabilistic solutions to the biomagnetic inverse problem. Inverse Problem 1990;6(523):542.

Ioannides A, Taylor J, Liu LC, Gross J, Muller-Gartner H. The influence of stimulus properties, complexity and contigency on the stability and variability of ongoing and evoked activity in human auditory cortex. Neuroimage 1998;8:149–162.

Ioannides A, Liu LC, Kwapien J, Drozdz S, Streit M. Coupling of regional activations in a human brain during an object and face affect recognition task. Hum Brain Mapp 2000;11:77–92.

Ioannides A, Kostopoulos G, Laskaris N, Liu L, Shibata T, Schellens M, Poghosyan V, Khurshudyan A. Timing and connectivity in the human somatosensory cortex from single trial mass electrical activity. Hum Brain Mapp 2002;15(4):231–246.

Jain A, Dubes R. Algorithms for clustering data. New Jersey: Prentice Hall, 1988. pp. 55–141.

Jansen B, Nyberg H, Zouridakis G. Selective averaging of evoked potentials using trajectory-based clustering. Methods Inform Med 1994;33(1):49–51.

Karakas S, Erzengin O, Basar E. A new strategy involving multiple cognitive paradigms demonstrates that ERP components are determined by the superposition of oscillatory responses. Clin Neurophysiol 2000;111:1719–1732.

Kowalik Z, Schnitzler A, Freund H, Witte O. Local Lyapunov exponents detect epileptic zones in spike-less interictal MEG recordings. Clin Neurophysiol 2001;112:60–67.

Lachaux JP, Rodriguez E, Martinerie J, Varela F. Measuring phase synchrony in brain. Hum Brain Mapp 1999;8:194–208.

Lange D, Siegelmann H, Pratt H, Inbar G. Modeling and estimation of single evoked brain potential components. IEEE Trans Biomed Eng 1997;44(9):791–799.

Lange D, Pratt H, Inbar G. Overcoming selective ensemble averaging: unsupervised identification of event-related brain potentials. IEEE Trans Biomed Eng 2000;47:822–826.

Laskaris N, Ioannides A. Exploratory data analysis of evoked response single trials based on minimal spanning tree. Electroenceph clin Neurophysiol 2001;112:698–712.

Laskaris N, Fotopoulos S, Papathanasopoulos P, Bezerianos A. Robust moving averages, with Hopfield neural network implementation, for the monitoring of evoked potential signals. Electroenceph clin Neurophysiol 1997;104(2):151–156.

Lee Y, Zhu Y, Xu Y, Shen M, Zhang H, Thakor N. Detection of nonlinearity in the EEG of schizophrenic patients. Clin Neurophysiol 2001;112:1288–1294.

Leocani L, Toro C, Zhuang P, Gerloff C, Hallett M. Event-related desynchronization in reaction time paradigms: a comparison with event-related potentials and corticospinal excitability. Clin Neurophysiol 2001;112:923–930.

Liu L, Ioannides A. A correlation study of averaged and single trials MEG signals: the average describes multiple histories each in a different set of single trials. Brain Topogr 1996;8(4):385–396.

Liu L, Ioannides A, Muller-Gartner H. Bi-hemispheric study of single trial MEG signals of the human auditory cortex. Electroenceph clin Neurophysiol 1998;106:64–78.

Makeig S, Westerfield M, Jung T-P, Enghoff S, Townsend J, Courchesne E, Sejnowski T. Dynamic brain sources of visual evoked responses. Science 2002;295:690–694.

Makela J, Hamalainen M, Hari R, McEvoy L. Whole-head mapping of middle latency auditory evoked magnetic fields. Electroenceph clin Neurophysiol 1994;92:414–491.

Mardia K, Kent J, Bibby J. Multivariate analysis, London: Academic Press, 1979.

Meng X, Xu J, Gu F. Generalized dimension of the intersection between EEGs. Biol Cybern 2001;85:313–318.

Pritchard W, Duke D. Measuring 'Chaos' in the brain: a tutorial review of EEG dimension estimation. Brain Cogn 1995;27:353–397.

Raz J, Turetsky B, Fein G. Confidence intervals for signal-to-noise ratio when a signal embedded in noise is observed over repeated trials. IEEE Trans Biomed Eng 1988;8:646–649.

Rulkov N, Sushchik M, Tsimring L, Abarbanel H. Generalized synchronization of chaos in directionally coupled chaotic systems. Phys Rev E 1995;51:980–994.

Schiff S, So P, Chang T, Burke R, Sauer T. Detecting dynamical interdependence and generalized synchrony through mutual prediction in a neural ensemble. Phys Rev E 1996;54:6708–6724.

Tass S, Rosenblum M, Weule J, Kurths J, Pikovsky A, Volkmann J, Schnitzler A, Freud HJ. Detection of n:m phase locking from noisy data: application to magnetoencephalography. Phys Rev Lett 1998;81(15):3291–3294.

Tenenbaum J, Silva V, Langford J. A global geometric framework

for non-linear dimensionality reduction. Science 2000;290:2319–2323.

Wackermann J, Matousek M. From the "EEG age" to a rational scale of brain electric maturation. Electroenceph clin Neurophysiol 1998;107(6):415–421.

Zouridakis G, Boutros N, Jansen B. A fuzzy clustering approach to study the auditory P50 component in schizophrenia. Psychiatry Res 1997a:169–181.

Zouridakis G, Jansen B, Boutros N. A fuzzy clustering approach to EP estimation. IEEE Trans Biomed Eng 1997b;44:673–680.